NeuroImage 100 (2014) 395–404

Contents lists available at ScienceDirect

NeuroImage

journal homepage: www.elsevier.com/locate/ynimg

Cross-validation of serial optical coherence scanning and diffusion tensor imaging: A study on neural fiber maps in human medulla oblongata

Hui Wang [a], Junfeng Zhu [b], Martin Reuter [c,d], Louis N. Vinke [c], Anastasia Yendiki [c], David A. Boas [c], Bruce Fischl [c,d], Taner Akkin [a,*]

[a] Department of Biomedical Engineering, University of Minnesota, Minneapolis, MN 55455, USA
[b] Department of Industrial and Systems Engineering, University of Minnesota, Minneapolis, MN 55455, USA
[c] Athinoula A. Martinos Center for Biomedical Imaging, Department of Radiology, Massachusetts General Hospital, Harvard Medical School, Charlestown, MA 02129, USA
[d] Computer Science and Artificial Intelligence Laboratory, Massachusetts Institute of Technology, Cambridge, MA 02139, USA

ARTICLE INFO

Article history:
Accepted 12 June 2014
Available online 20 June 2014

Keywords:
Validation
Diffusion magnetic resonance imaging
Optical coherence tomography
Polarization
Fiber orientation
Anisotropy
Human brain
Connectome

ABSTRACT

We established a strategy to perform cross-validation of serial optical coherence scanner imaging (SOCS) and diffusion tensor imaging (DTI) on a postmortem human medulla. Following DTI, the sample was serially scanned by SOCS, which integrates a vibratome slicer and a multi-contrast optical coherence tomography rig for large-scale three-dimensional imaging at microscopic resolution. The DTI dataset was registered to the SOCS space. An average correlation coefficient of 0.9 was found between the co-registered fiber maps constructed by fractional anisotropy and retardance contrasts. Pixelwise comparison of fiber orientations demonstrated good agreement between the DTI and SOCS measures. Details of the comparison were studied in regions exhibiting a variety of fiber organizations. DTI estimated the preferential orientation of small fiber tracts; however, it didn't capture their complex patterns as SOCS did. In terms of resolution and imaging depth, SOCS and DTI complement each other, and open new avenues for cross-modality investigations of the brain.

Introduction

Diffusion magnetic resonance imaging (dMRI) has revolutionized our understanding of structural connections in humans. The technique provides a unique solution to noninvasively visualize white matter fiber bundles over macroscopic distances in the living brain. dMRI captures the anisotropic diffusion of water molecules in the brain which run preferentially along the direction parallel to the axonal axes, and can be used to infer fiber organization and orientation. Recent technical developments have improved the spatial resolution to sub-millimeter scale and enabled high angular resolution imaging which describes the human brain with unprecedented details. dMRI has been proven to be valuable in clinical neuroscience (Fields, 2008; Thomason and Thompson, 2011), with studies showing that an array of disorders may have corresponding connectional components, including Alzheimer's disease (Kitamura et al., 2013; Wang et al., 2007), schizophrenia (Miyata et al., 2007; Rosenberger et al., 2012; Schmitt et al., 2011; Voineskos et al., 2010), autism spectrum disorders (Nair et al., 2013; Pollonini et al., 2010), major depression (Maller et al., 2010; Tham et al., 2010), and dyslexia (Koyama et al., 2013; Pugh et al., 2000; Vandermosten et al., 2012).

While there have been a number of neuroscientific and clinical applications of dMRI, the systematic validation of the dMRI technique for evaluating microstructural properties and connectivity in the human brain remains incomplete. Although light microscopy is able to visualize single axons, axonal tracking is extremely labor intensive, and cannot realistically be carried out for multiple fascicles traversing many centimeters of brain tissue through the white matter. Traditional validations by histology are divided into two realms: 1) neural tract tracers have been injected into local regions, and compared with selected tracks by dMRI tractography (Caminiti et al., 2013; Harsan et al., 2013; Seehaus et al., 2013); and 2) quantitative information have been derived by digital signal processing of myelin stained images and compared with dMRI orientation (Budde et al., 2011; Choe et al., 2012; Hansen et al., 2011; Leergaard et al., 2010). Those studies are predominantly performed on 2D slices. Early three-dimensional (3D) histological validation has proven to be difficult and has resulted in a relatively low correlation with dMRI tracks (Dauguet et al., 2007). Using multi-step registrations, Jbabdi et al. (2013) reported both agreements and dissociations between neural tracing trajectories and dMRI tractography on the organizations of ventral prefrontal fibers in macaque monkey. Polarized light imaging (Axer et al., 2011) has

* Corresponding author at: 7-105 Hasselmo Hall, 312 Church Street SE, Minneapolis, MN 55455, USA.
E-mail address: akkin@umn.edu (T. Akkin).

http://dx.doi.org/10.1016/j.neuroimage.2014.06.032
1053-8119/

recently been proposed as an alternative technique for imaging fiber orientation, as it provides 3D orientation information with an isotropic voxel size of approximately 100 μm. However, the technique requires tissue slicing before the imaging, which makes inter-slice tracking of fiber bundles difficult and is prone to registration errors due to distortions intrinsic to cutting and mounting of large tissue sections.

The development of optical coherence tomography (OCT) (Huang et al., 1991) has shown promise for depicting fiber tracts in the central and peripheral nervous system (Arous et al., 2011; Leahy et al., 2013; Wang et al., 2011) and creating high-resolution brain images that have been correlated with histology (Assayag et al., 2013; Magnain et al., 2014). OCT is a depth-resolved imaging technique that generates cross-sectional images and 3D reconstruction of tissue microstructures. By integrating a tissue slicer with multi-contrast OCT, serial optical coherence scanner (SOCS) provides insight into large-scale brain imaging with microscopic resolution (Wang et al., 2014). SOCS enables a comprehensive 3D reconstruction of the brain and supports quantitative assessments of fiber architecture and orientation with intrinsic optical contrasts. Reflectivity is the conventional OCT contrast that measures the intensity of back-scattered light, and is sensitive to the variations of refractive index in tissue. On the other hand, polarization sensitive OCT (de Boer et al., 1997) utilizes an optical property called birefringence that originates from structural anisotropy. The birefringent tissues such as muscle, tendon and nerve have an optic axis on a plane orthogonal to the direction of light propagation. Because refractive indices for light polarized parallel and perpendicular to the optic axis are different (the difference is defined as birefringence), the polarization state of light traveling in such a tissue changes due to a delay between the orthogonal polarization components. The delay, known as retardance, is equivalent to the birefringence multiplied by the distance light travels, and it can be represented by phase as one wavelength corresponds to 360°. Brain imaging with SOCS showed that the reflectivity contrast portrays the morphology, and the polarization contrasts primarily probe myelinated nerve fibers in the white matter: the retardance delineates the architecture of nerve fibers, and the optic axis orientation quantifies the in-plane fiber orientations (Wang et al., 2011). In addition to the sectioning capability with multiple optical contrasts, the high acquisition speed of SOCS makes it appealing for macroscopic brain imaging in humans and non-human primates.

In this paper, we present cross-validation of SOCS and diffusion tensor imaging (DTI), which is a dMRI technique, on a postmortem human medulla sample. We establish a strategy that allows registration between 3D datasets of DTI and SOCS at high resolution. The white matter structures in the medulla are correlated on co-registered images. The fiber orientation maps produced by these modalities are compared. This study shows the potential for a cross-modality investigation of structural connectivity in normal and diseased brain.

Materials and methods

Tissue

Tissue sample was taken from the right hemisphere of a 60 year old male initially fixed in 10% buffered formalin beginning 14 hours postmortem for 2 months, and then subsequently stored in 4% periodate–lysine–paraformaldehyde (PLP) prior to and during data collection. Brain tissue was obtained from the Neuropathology Department at the Massachusetts General Hospital and is considered to be cognitively normal. A block of tissue, with an approximate size of 11 × 15 × 30 mm^3, containing the medulla oblongata was removed from the right brainstem which fit within a 28 mm inner diameter (ID) plastic cylinder. MRI human brain tissue experiments were approved by an Institutional Review Board at Massachusetts General Hospital. After the acquisition of DTI data at Massachusetts General Hospital, the sample was transferred to University of Minnesota for optical imaging.

DTI data acquisition

DTI data was acquired using a Bruker BioSpec Avance system (4.7 T/40 magnet, 12 cm bore, 40 G/cm gradients) at a 300 μm isotropic spatial resolution. The acquisition employed a 3D spin-echo sequence (TR/TE = 320/28, $\delta = 7$ ms, $\Delta = 10.4$ ms, matrix size = 256 × 96 × 96). The scan included diffusion-weighted images acquired with a b-value of 4032 s/mm^2 and 20 non-collinear diffusion-encoding directions, and two images acquired with a b-value of 0 s/mm^2. Total scan time was 18 h.

Radio frequency coil

A custom-built transmit/receive solenoid coil was designed to minimize the distance between the blocked sample in the plastic cylinder container and the surrounding coil, with an inner diameter of 30 mm and active length of 70 mm resulting in 5 turns of the copper coil element.

DTI post-processing

Diffusion tensor estimation and tractography was performed using the Diffusion Toolkit (Ruopeng Wang, Van J. Wedeen, TrackVis.org, Martinos Center for Biomedical Imaging, Massachusetts General Hospital). The Fiber Assignment by Continuous Tracking (FACT) algorithm (Mori et al., 1999) was used with a maximum bending angle of 35°. The tensor maps were used to estimate the apparent diffusion coefficient, fractional anisotropy (FA), and fiber orientations.

SOCS imaging

SOCS integrates a multi-contrast OCT and a Vibratome tissue slicer (Wang et al., 2014). The multi-contrast OCT is a spectral-domain polarization-maintaining-fiber (PMF) based technique (Wang et al., 2010) that is capable of making intensity, phase and polarization sensitive measurements. The light source is a super-luminescence diode (central wavelength: 840 nm; bandwidth: 50 nm) yielding an axial (z-axis) resolution of 5.5 μm in tissue. A scan lens (focal length: ~36 mm) providing an estimated lateral (x/y-axis) resolution of ~15 μm is employed in the sample arm for consistent imaging quality over a large area. The acquisition speed for a depth profile (A-line) is set to 25 kHz. This is determined by a line scan camera recording interference related spectral oscillations on the orthogonal PMF channels. Inverse Fourier transform of the spectra in k (wave number) space yields the complex depth profiles in the form of $A_{1,2}(z)exp\{i\Phi_{1,2}(z)\}$, where the subscripts represent the polarization channels. The reflectivity $R(z)$, phase retardance $\delta(z)$ and relative axis orientation $\theta'(z)$ along depth z are extracted from the magnitudes and phases of the complex depth profiles as $R(z) \propto A_1(z)^2 + A_2(z)^2$, $\delta(z) = \arctan(A_1(z)/A_2(z))$, and $\theta'(z) = (\phi_1(z) - \phi_2(z))/2$, respectively. Construction and operation details of the imaging system can be found in Wang et al., 2010.

The medulla sample was cropped into a 2 × 1 × 0.7 cm^3 block (in xyz) and mounted on a vibratome slicer (Leica Microsystems, Bannockburn, IL) positioned under the scanner. One volumetric scan (optical section) contained 300 cross-sectional frames with 1000 A-lines in each frame. Each scan covered a 3D volume of 7 × 7 × 1.78 mm^3 and produced images with a voxel size of 7 × 23 × 3.47 μm^3. Eight scans were performed to cover the entire sample surface (2 cm × 1 cm). The scan head was repositioned between the adjacent sections, which had a 15% overlap to aid post-processing. One of these scans was also used for calibrating the axis orientation contrast, since a retarder with a known axis was placed next to and imaged together with the medulla sample. After imaging the superficial region, a 150 μm thick tissue slice was removed from the top surface, allowing for deeper regions to be exposed to light. The physical slice thickness was less than the useful imaging

depth to ensure 3D reconstruction with satisfactory signal-to-noise ratio at all depths. The sections of consecutive slices were imaged in reverse order to minimize the lateral repositioning of the scan head, which also facilitates successful stacking of the slices. The imaging and then slicing procedure was repeated 45 times until the entire tissue block was scanned, resulting in the recording of a total of 360 optical sections. The experimental setup, the scanning procedure and the reconstructions of 2D and 3D images are illustrated in Fig. 1.

SOCS image reconstruction and post-processing

To resemble the view of block-face microscopy, the volumetric data of reflectivity, retardance and axis orientation contrasts were projected onto the xy-plane for each optical section, forming the *en-face* images. In such a way, surface and subsurface features are unveiled on the images (Fig. 1C). The pixel intensity in *en-face* reflectivity and retardance images was computed by taking the corresponding mean value along the depth direction. The pixel intensity in *en-face* orientation images was determined by the peak of a histogram formed by binning the orientation values along depth into 2° intervals. The depth range used in calculations matches the physical slice thickness.

En-face views of eight optical sections were stitched to construct a slice. The *en-face* retardance images were chosen as those displaying the most remarkable features in the medulla with high contrast. An algorithm based on the Fourier shift theorem computed the translations between all image pairs, found the best overlaps and produced a globally optimized configuration for the whole image (Preibisch et al., 2009). The operation was performed by Fiji software (http://pacific.mpi-cbg.de/). The same registration was then applied to stitch the *en-face* reflectivity and axis orientation images.

The 3D reconstruction of the medulla sample was achieved by stacking the *en-face* images of the slices (Fig. 1D). The imaging procedure allows for precise alignment of the slices without further registration. However, lateral positions of the slices can be fine-tuned by referencing the sections that were imaged without the lateral repositioning of the scan head.

The optic axis orientation represents the axis of anisotropy in the plane perpendicular to the illuminative beam. This measure indicates the in-plane orientation of nerve fibers; however, it bears an offset that needs to be removed to achieve physical fiber orientation. The offset originates from an arbitrary delay between the optical paths of the two PMF channels, which varies with environmental factors such as movement of reference or sample arm fibers and temperature change. To obtain the absolute orientation of nerve fibers, a retarder film was placed next to the tissue, and a small portion of it was covered in one of the eight scans. The offset was derived by subtracting the measured and set orientations of the film axis, and removed from the measured axis orientation of the tissue in that section. Other sections of the slice were corrected serially by matching the fiber orientations within the overlap regions.

Co-registration between DTI and SOCS

As the coordinate space of SOCS imaging is different than that of the DTI data, co-registration between the two imaging modalities is crucial for the accuracy of orientation comparison. The co-registration involves two steps: (1) performing image registration to align the DTI to the optical images, and (2) applying the rotational component of this registration to the orientation vectors derived from dMRI to map them to the coordinate system of the optical images.

The spatial registration was performed using DTI FA and SOCS retardance images, as most features including the gray and white matter boundary and the architectures of the white matter fiber tracts are captured in the two contrasts (Basser, 1995; Wang et al., 2011). The DTI dataset was mapped into the SOCS space and interpolated to match the voxel size of SOCS. After an initial manual rotation and cropping on the 3D dataset of FA, a rigid transformation (translation and rotation) followed by an affine alignment (translation, rotation, scaling and shearing) was estimated and applied to the FA block using a modification of the symmetric registration procedure described in Reuter et al. (2010) with normalized mutual information as the cost function.

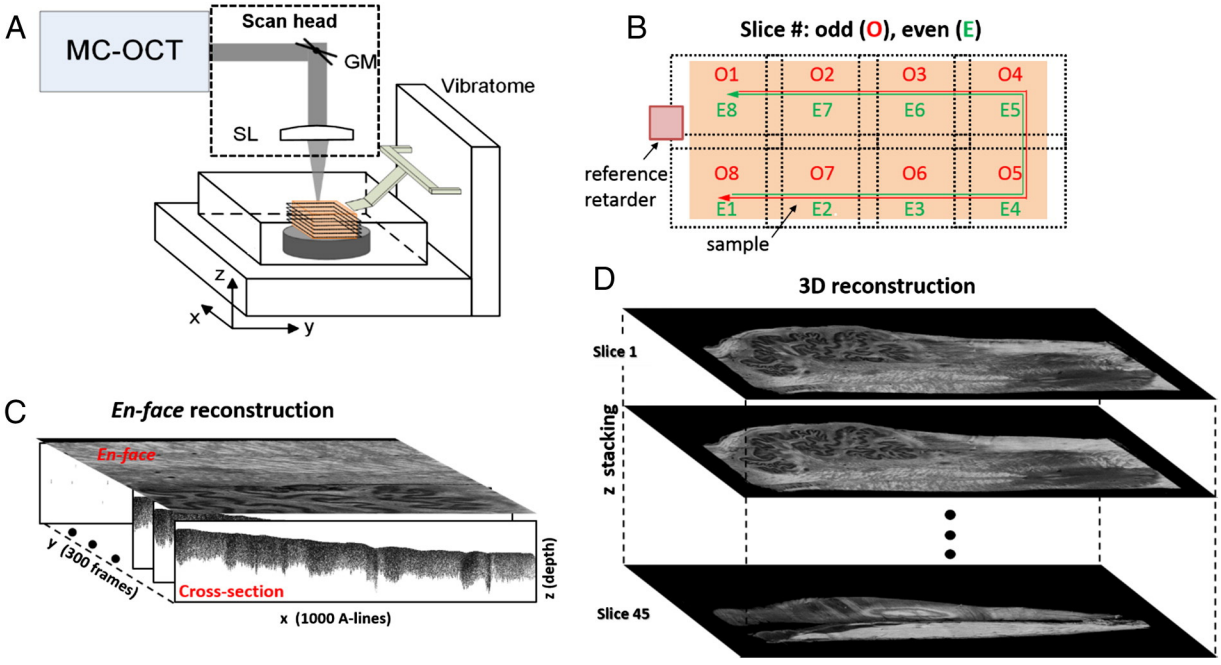

Fig. 1. Acquisition and reconstruction of SOCS images. A. SOCS integrates a vibratome into MC-OCT. The scan head performs a raster scan with a pair of galvos (GM), and it is movable. SL: scan lens. B. The lateral plane is divided into eight regions with 15% overlap between the adjacent scans. To cover the entire surface, the scan head is positioned over these regions in the order given. O and E refer to odd and even numbered slices, respectively, whose optical sections are imaged in reverse order (red and green arrows). C. *En-face* image reconstruction. One of eight optical sections of a slice is shown. The *en-face* image is constructed by projecting the optical section onto the xy-plane. D. 3D reconstruction from *en-face* images. Individual slices, each containing eight optical sections, are stacked in z to form a 3D representation of the sample.

After spatial alignment, the DTI orientation vectors were reoriented to map onto SOCS coordinates. Vector reorientation was performed using the transformation that we obtained with the image registration procedure described above. First, the registration was applied to the tensor volumes to map them to the coordinate space of the SOCS orientation images. Second, the rotation matrix extracted from the registration transform was applied to reorient the tensors. The primary eigenvectors were extracted from the registered diffusion tensor maps. Because the optic axis orientation is defined on the xy-plane, the DTI vectors were projected onto the en-face plane of SOCS. The advantage of this registration strategy is that it enables a voxelwise co-evaluation of the entire sample with high resolution.

Results

Optical images

Fig. 2 displays the *en-face* images of a medulla slice composed of eight (2×4) laterally scanned optical sections roughly parallel to the coronal plane. The *en-face* reflectivity image emphasizes the layer of the inferior olivary nucleus with high scattering, which may contain a high-density of cell bodies (red arrows). The accessory olivary nuclei are also recognizable (yellow arrow). Those nuclei appear dark on the retardance images with no indicative birefringence. The brightness of the white matter varies on the reflectivity images, as the fiber orientation with respect to the direction of the illuminative beam (inclination angle) affects the backscattering of light. However, textures within gross white matter are distinguishable as highlighted in the magnified region on the right. The *en-face* retardance image emphasizes the white matter fiber bundles with detectable birefringence. The brightest regions are seen where fiber tracts are densely packed in a uniform direction and aligned parallel to the *en-face* plane. Distinct features such as the reticularis alba and fiber clusters at the pyramid decussation (green arrow) are visible regardless of lower retardance values. The inclination angle affects the retardance measurement as well (Larsen et al., 2007). Fiber tracts running through the plane with large inclination angles appear dark, but the effect is less severe than that on the reflectivity image. Small fibers traversing the olivary nuclei are observed on the magnified region as indicated by the arrows. The size of the individual tracts is estimated to be about 20–30 μm. Using color-coded channels, reflectivity and retardance images are overlaid for a better visualization of the structure layout and spatial interactions. The stacking order is reversed in the zoomed-in region to reveal the pattern of fiber tracts crossing with each other and running through the nuclei region. We selected the retardance contrast for spatial registration with the DTI data, because of its ability to highlight the white matter tracts and reveal features of their architecture.

The *en-face* optic axis orientation maps in Fig. 3 show fiber orientations on the coronal plane. The colors represent the fiber directions as shown on the color wheel. The brightness of colors is determined by the *en-face* retardance values. As expected from anatomy, the majority of white matter bundles are aligned along the superior-inferior (x-axis) direction. However, more complex fiber architecture can be seen at the pyramid decussations and in the inferior olive. The optic axis orientation traces the directional trajectory of small tracts of tens of micrometers, and detects the individual directions of the intricate networks. The high-resolution quantitative assessment sets the basis for a direct correlation with the DTI contrasts.

Co-registration of DTI and SOCS images

The datasets of DTI and SOCS were co-registered by utilizing the contrasts of FA in DTI and the retardance in SOCS, as both contrasts emphasize the fiber bundles in white matter. Supplemental Video S1 shows the co-registered retardance and FA images of the medulla sample on the xy-plane. Fig. 4 demonstrates representative views on

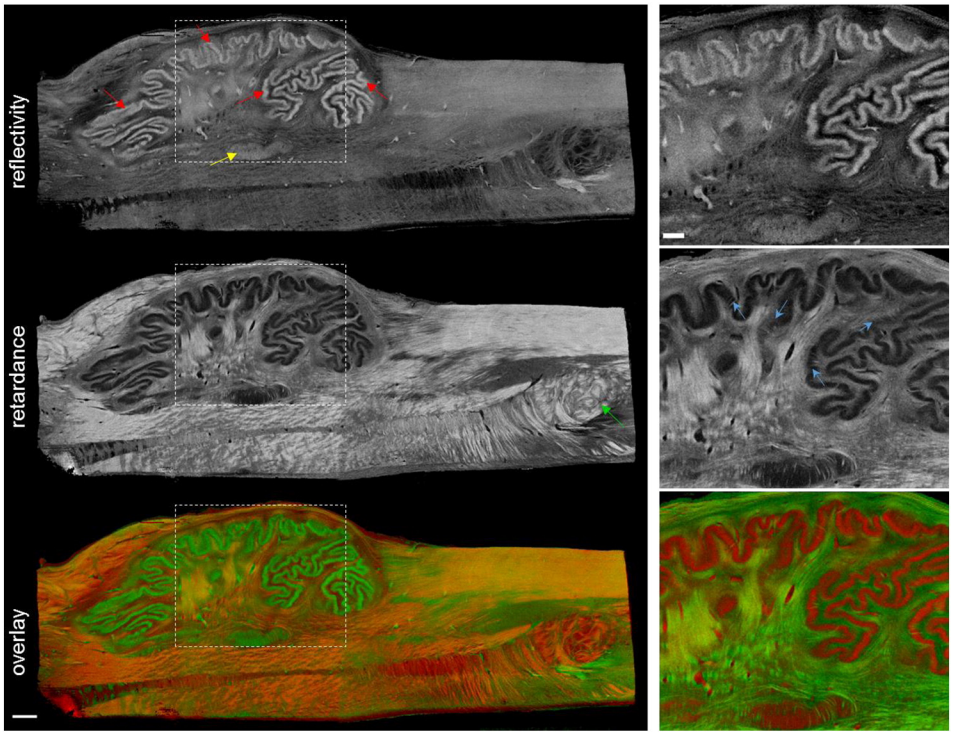

Fig. 2. *En-face* reflectivity and retardance images of the medulla oblongata. Left: A slice composed of eight (2×4) lateral scans. Reflectivity highlights the inferior olivary nucleus layer (red arrows) and the accessory olivary nuclei (yellow arrow). Retardance probes the white matter region. Green arrow: pyramid decussation. The overlay is merged by color channels (red: retardance; green: reflectivity). Right: Images elaborate the details in the dotted box. Arrows on the retardance image indicate small fiber tracts transversing the inferior olive nucleus. The colors of the overlay are switched to underscore the spatial interactions within fiber tracts and between the tracts and the nuclei. Scale bars: left, 1 mm; right, 500 μm.

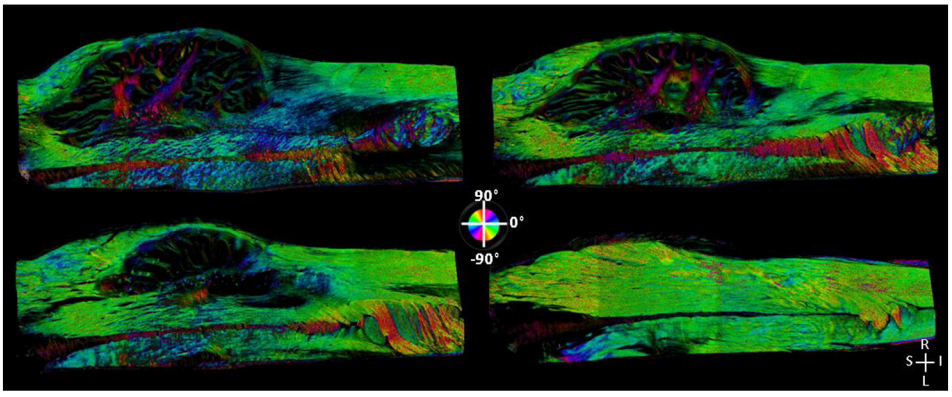

Fig. 3. *En-face* optic axis orientation maps produced by SOCS quantitatively depict in-plane fiber orientations in the medulla. Each map is composed of eight (2×4) serial scans. The color wheel shows the orientation values ranging between $-90°$ and 90°. The brightness of colors in the images is determined by the *en-face* retardance values.

the orthogonal planes. The registered images exhibit appreciated similarity on all the orthogonal planes. The fiber structures in the inferior olive are less distinctive on FA images (top) due to a limited spatial resolution of DTI. These fiber tracts, as estimated from the retardance images, are less than 500 μm in diameter, which is comparable to the DTI voxel size. Fig. 4 also shows color-merged binary images that are obtained by applying thresholds on retardance (22.5°) and FA (0.15) images. Tissue boundaries on the blended images present a close match, attesting to minimal distortion due to serial sectioning of SOCS. Small misalignments are seen on the inferior and superior edges, which might be attributed to an excessive shear transformation during registration. These images also indicate a general agreement between the white matter borders. Discrepancies exist in detailed structures (e.g. the inferior olive), which might originate from slicing artifacts, registration errors and a mismatch in the spatial resolutions.

To assess the quality of co-registration, we computed the correlations of the 3D datasets of FA and retardance using three measures: Dice's coefficient of the tissue masks, Dice's coefficient of the white matter masks, and Pearson's correlation coefficient. The Dice's coefficient measures the spatial overlap of two point sets, ranging in value from 0 meaning no overlap, to 1 indicating perfect overlap. The Dice's coefficient on tissue mask was 0.96, indicating a nearly perfect overlap of the co-registered datasets. Dice's coefficient of the white matter masks and Pearson's coefficient were both 0.90, signifying appreciable agreements in the co-registered white matter structures. The Pearson's coefficient indicates both the precision of alignment and the correlation of contrast between the two dataset, since it takes the intensity of images into account. All three measures suggest successful co-registration of the images from the two modalities. Because the voxel size of SOCS *en-face* stack is anisotropic, we further examined whether this anisotropy along lateral and axial axes could unevenly affect the registration quality. We calculated the Pearson's correlation coefficients in every section on individual viewing planes across the whole sample. The correlation coefficients are estimated to be 0.88 ± 0.05, 0.89 ± 0.03, and 0.80 ± 0.05 (mean $\pm$ standard deviation) for xy-, xz- and yz-planes, respectively. The results indicate that the quality of registration is comparable on different viewing planes.

FA and retardance contrasts

Although both FA and retardance highlight the white matter, the underlying physics of the contrasts are different: FA represents the anisotropy of water diffusion in tissue, while retardance originates from tissue birefringence. As the nerve fiber tracts influence both measures greatly, further comparison of the FA and retardance images is of interest. Fig. 5A shows the co-registered retardance and FA images in four slices. We selected five regions of interest (ROIs) within the white matter and compared the features across the two imaging contrasts. ROI-1 is located in dense fiber bundles of the pyramid which exhibits a high brightness albeit a lack of detailed features. ROI-2 is placed in the reticularis alba with meshing patterns visible on the retardance. ROI-3 is on the fiber tracts beside the olive with lower density. ROI-4 contains small fibers in the inferior olive with complicated interacting orientations. ROI-5 is located at the median fissures between the left and right medulla. The ROIs are included in multiple slices where individual structures are clearly visible.

The mean values of retardance and FA are plotted against each other for all selected ROIs in Fig. 5B. The data follow a positive trend for ROIs 1–4. This indicates that greater anisotropy in DTI correlates with higher birefringence due to nerve fibers running parallel with each other. Lower anisotropy may be due to lower fiber density or myelin content, or complex geometries such as crossing, kissing or fanning fibers. The relationship differs in the median fissures (ROI-5), where the FA is relatively high and the retardance is relatively low. Therefore, the anisotropy of water diffusion can be large without the presence of myelinated fibers affecting the measured retardance. It should also be

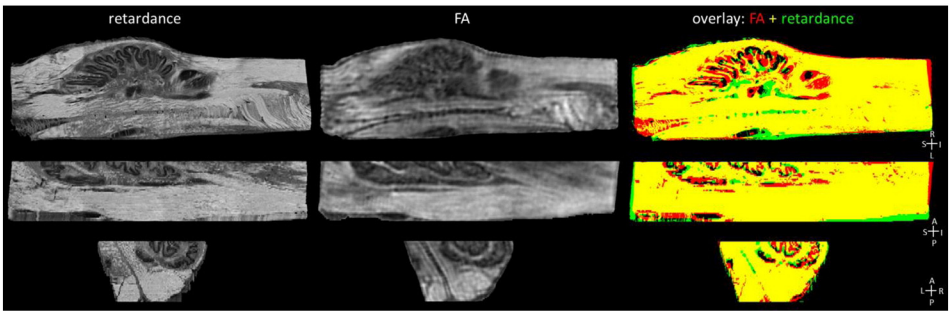

Fig. 4. Spatial co-registration of SOCS and DTI images. Retardance (left column) and FA (middle column) images are shown on axial (top row), sagittal (middle row) and coronal (bottom row) views. Color-coded binary images of the white matter regions indicate the quality of registration (green: retardance; red: FA; yellow: the overlap).

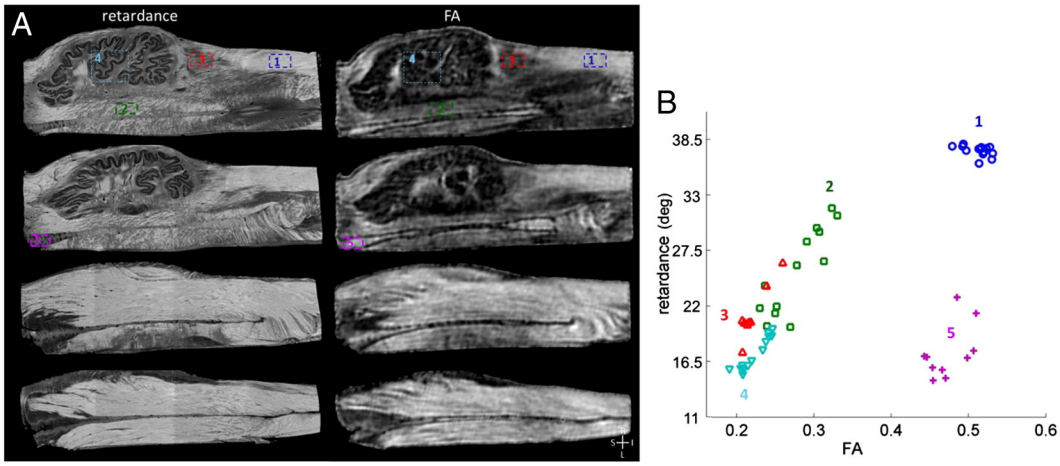

Fig. 5. Correlation between retardance and FA images. A. Representative images of retardance (left) and FA (right) for four medulla slices. Five ROIs are selected on varied structures. The ROIs are across multiple slices where specific structures are clearly visible. B. The scatter plot relates the mean values of retardance and FA in selected ROIs with color coding. Each point represents an ROI within a slice.

mentioned that, the inclination angle of fibers with respect to the xy-plane could reduce the retardance. This is not an issue for dMRI, where water diffusion is measured along multiple directions.

Fiber orientations

The quantitative assessment of fiber orientation in SOCS enables a direct comparison with DTI orientation. Supplemental Video S2 shows the SOCS and DTI orientation images of the medulla sample. Fig. 6 demonstrates the orientation maps for four representative slices. The orientation maps share the same color coding given in the color wheel. The brightness of colors on SOCS and DTI images is adjusted by the local retardance and FA values, respectively. The color patterns hold substantial similarity between the co-registered images. This also suggests successful registration. Precise matches are seen in gross white matter regions bearing uniform directions, regularly grouped fiber bundles in the pyramid running at the decussation, and large fiber tracts located in the inferior olive. In contrast, discrepancies are observed where small fiber bundle regions introduce noisy patterns into the DTI maps. This is apparent in the olive region where the size of fiber bundles is comparable to the DTI resolution.

Pixel-wise subtraction of the DTI and SOCS orientation maps yields the mismatch between the measurements of these imaging modalities. Three sets of FA and retardance thresholds were applied to select the white matter regions for comparisons. Fig. 7A shows the orientation mismatches on two representative sections of the medulla sample,

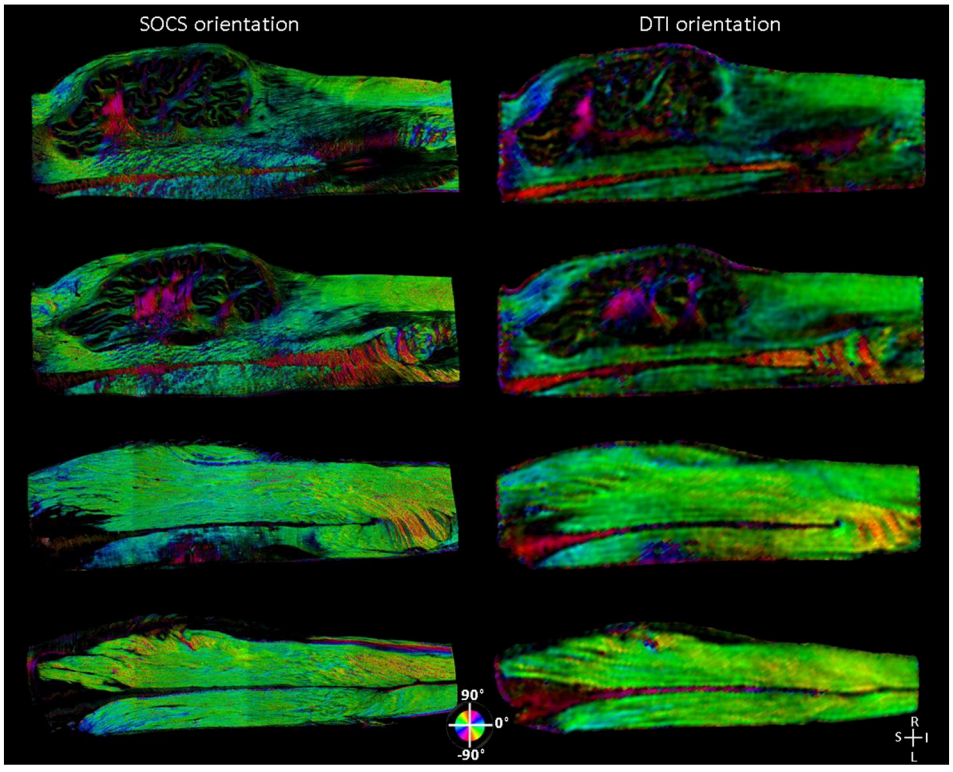

Fig. 6. Co-registered SOCS (left) and DTI (right) fiber orientation maps for four medulla slices. The color wheel indicates the orientations of fiber tracts. The brightness on SOCS and DTI maps is controlled by retardance and FA values, respectively.

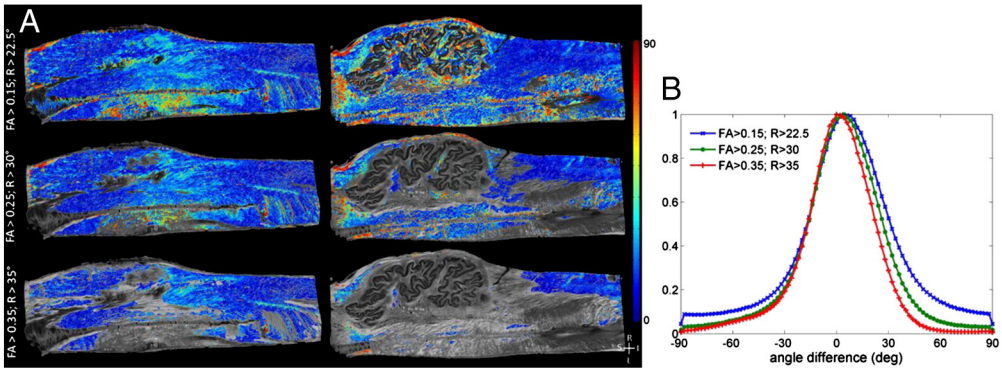

Fig. 7. Pixel-wise comparison of the DTI and SOCS orientation maps. A. The orientation mismatch (absolute difference) is overlaid on gray-scale retardance images for two representative slices (left and right columns). Fiber bundles in white matter regions are selected by three sets of thresholds — top row: FA > 0.15, retardance > 22.5°; middle row: FA > 0.25, retardance > 30°; bottom row: FA > 0.35, retardance > 35°. Color bar: 0° — 90°. B. Normalized histograms of the pixel-wise orientation difference (bin width: 2°). The pixels are selected from all slides by applying the thresholds. The mean differences are at 5.4°, 3.3° and 0.1°, and the standard deviations are 32.5°, 26.3° and 22.6°, for increasing thresholds, respectively.

whose structure is given by gray-scale retardance images. In general, a convergence of co-registered orientations is seen in the majority of areas, indicating the general concordance between DTI and OCT measures. The lowest threshold pair (FA > 0.15 and retardance > 22.5°) covers almost all white matter in the medulla, and exposes areas with discrepancy in the orientation with distributed patches of hot colors. This includes borders of the white matter where registration errors may play an important role. Discrepancies gradually diminish with increasing thresholds, as the DTI and SOCS better describe the white matter regions and their orientation measurements become closer. The highest threshold pair (FA > 0.35; retardance > 35°) tends to select unidirectional fiber bundles that are aligned parallel to the SOCS *en-face* plane. As shown, this reveals the smallest difference between the orientation maps. Fig. 7B shows the normalized histograms of the pixel-wise orientation differences, which were obtained from all slices for each threshold pair. The bin-width was 2°. The mean values of the orientation difference are small for the three threshold pairs (5.4°, 3.3° and 0.1° from low to high thresholds). Similarly, the standard deviations of the distributions decrease as the thresholds increase (32.5°, 26.3° and 22.6°) indicating that the width of the distributions becomes narrower. Discrepancies may originate from the averaging effect of orientation estimation in DTI, the fiber tracts with large inclination angles that affect the optical signals, or the registration errors.

We further compared the fiber orientations in selected ROIs with varied architectures. Fig. 8A shows four ROIs on the co-registered orientation maps. ROI-1 contains densely packed fibers exhibiting high FA and retardance values. ROI-2 is a transition area where small fiber tracts with lower density are visible on the retardance image and the FA image has a correspondingly lower intensity. ROI-3 is above the inferior olive where the FA indicates greater anisotropy and the retardance image shows clustered fiber bundles aligned along a preferred direction in the xy-plane. ROI-4 is in the pyramid at the decussation where two groups of fiber bundles with different orientations are found. The ROIs are across multiple slices where specific structures are recognizable. Fig. 8B shows histograms of fiber orientations measured by SOCS and DTI (bin width: 5°). Fiber orientations in ROI-1 present the highest agreement, where SOCS orientation peaks at −35° and DTI orientation peaks at −30°. The histograms also have the narrowest width, indicating that the fiber bundles are aligned parallel with each other. Although fiber density is lower in ROI-2, the comparison still supports a good concordance, with SOCS peaking at −10° and DTI at −15°. Histograms of ROI-3 and ROI-4 show greater, yet fairly comparable

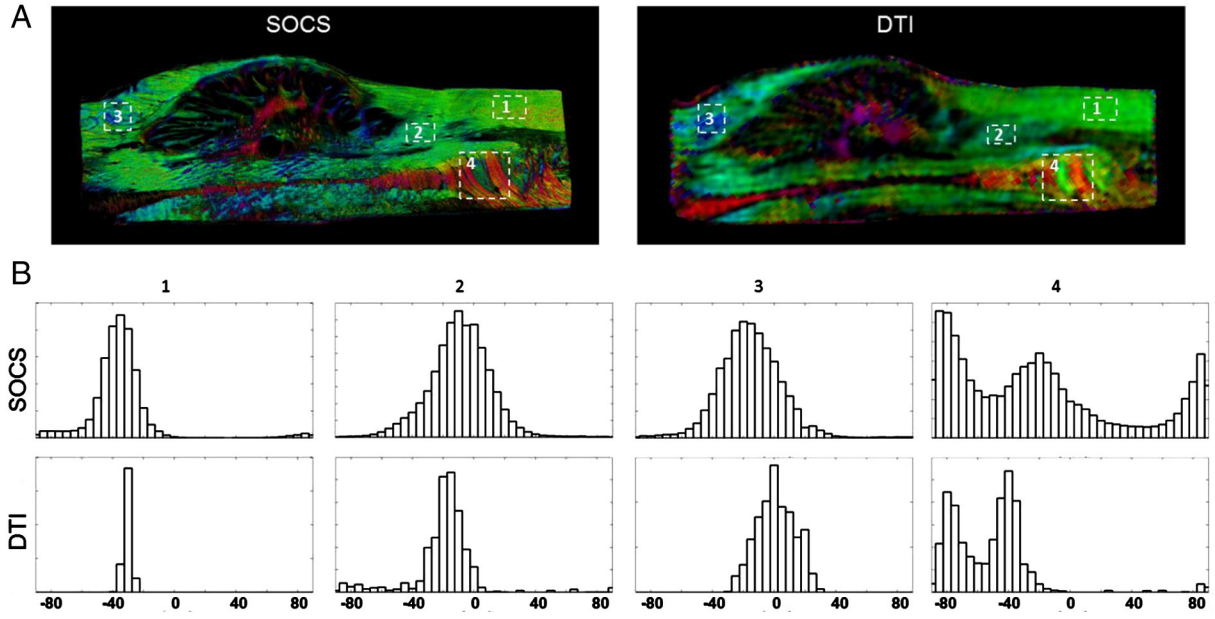

Fig. 8. Fiber orientations in ROIs. A. Four ROIs are shown on SOCS (left) and DTI (right) images. The color chart is the same as in Fig. 7. The ROIs are across multiple slices containing the specific features. B. Histograms of the orientations in the ROIs for SOCS (top) and DTI (bottom). Bin width is 5°.

differences within 20°. Broader distributions may suggest complex patterns within the ROIs. For instance, ROI-4 exhibits a bimodal distribution that arises from distinct fiber bundles in a larger volume. The orientation distributions of SOCS are broader than those of DTI in the selected ROIs. This may be due to the higher resolution of SOCS enabling it to reveal subtle orientation variations.

Despite the positive correlations between DTI and SOCS measures, there are complex fiber patterns that the DTI techniques cannot resolve. Fig. 9A provides two examples which are magnified ROIs marked on Fig. 9B. These ROIs contain fiber tracts smaller than 100 μm in diameter. The superior resolution of SOCS permits the description of these tracts, whereas pixelated patches are observed on DTI orientation images. The SOCS orientation in ROI-1a demonstrates three major groups present at the intersections, centered at 30°, −60° and 90°; whereas, the DTI orientation loses the differentiation of the crossing fibers. Moreover, delicate patterns of fiber crossing are visible by SOCS in ROI-1b, where the anisotropy on DTI is low due to the averaging of multiple orientations. The capabilities and limitations of the DTI technique can be further visualized in ROI-2 and ROI-3. At the pyramid decussation, the DTI is capable of estimating the preferential orientation of small fibers (yellow-orange patterns in lower ROI-2); however, it is not possible to resolve the multiple orientations present in fiber crossings. Similarly, the unidirectional fibers of median fissure appears to have the same orientation in DTI and SOCS images (Fig. 9C), but the inter-weaving fibers in ROI-3a are not represented by DTI. The fiber orientations in ROI-3a are analyzed for quantitative evaluation. The histogram for SOCS shows a side lobe centered at 70° in addition to the primary peak. In contrast, the fiber orientations by DTI have a more uniform distribution.

Discussion

This work presents co-validation of SOCS and DTI measurements using neural fiber pathways on a postmortem human medulla oblongata sample. We established a registration strategy that supports precise alignment of the 3D data from the two modalities, and accomplished direct comparison of white matter structures and fiber orientations at high resolution.

The multiple contrasts of SOCS describe the fiber tracts and the nuclei in the medulla from different perspectives. The polarization measures especially target white matter fiber tracts due to the birefringence property of axons. The *en-face* retardance stack delineates the architecture of fiber networks, which forms an analogy with the FA in DTI and sets the basis for cross-modality registration. 3D reconstruction of the macroscopic sample is accomplished by stitching and stacking multiple optical scans. Unlike validation with histology that requires complicated tissue processing and inter-slice registration, the registration procedure is straightforward and significant mechanical distortions are not observed. The quality of co-registration between 3D datasets of FA and retardance was remarkable as indicated by Dice's coefficients of 0.96 and 0.90 for tissue and white matter masks, respectively. As a result, SOCS shows a significant merit in comprehensive studies on macroscopic brain regions.

Although the underlying origins of the FA and retardance signals are different, the co-registered images of the entire sample exhibit remarkable similarities with a Pearson's correlation coefficient of 0.90. The microscopic resolution of SOCS enables a closer inspection of the neuroanatomical factors affecting the FA values. We found that high FA corresponds to high retardance where parallel fibers are densely

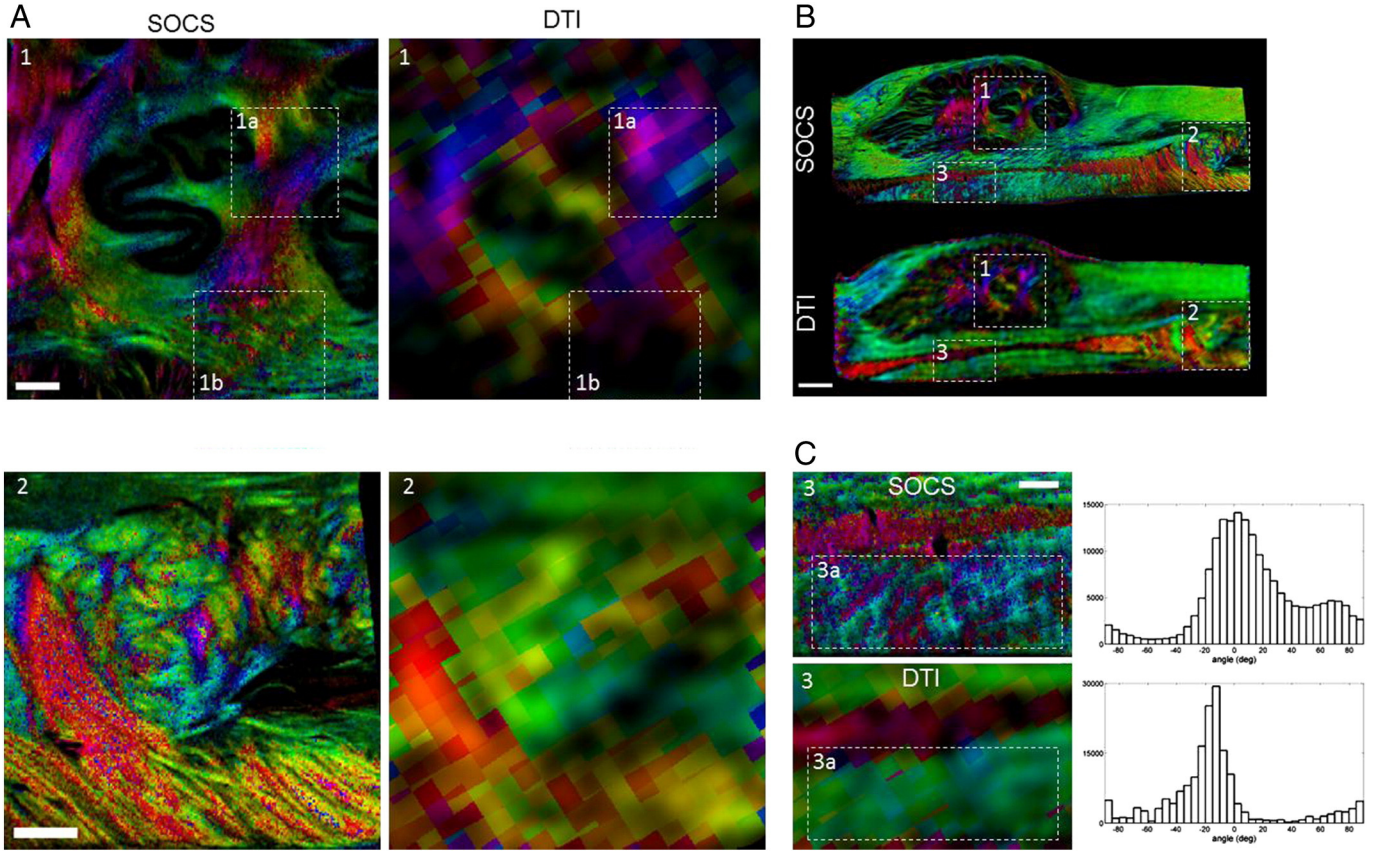

Fig. 9. Crossing fibers on SOCS and DTI orientation maps. A. Two magnified ROIs (ROI-1 and 2 in B) demonstrate complicated crossing patterns of fiber networks. SOCS images (left) clearly delineate individual fiber bundles with altered colors, while pixelated DTI images (right) lose track of subtle variations. B. SOCS and DTI orientation maps of the medulla slice showing the ROIs. C. Reticular patterns of crossing fibers by SOCS, and more homogeneous DTI representation. Histograms of orientations in ROI-3a (top: SOCS, bottom: DTI, bin width: 5°). Scale bar in A and C: 500 μm; scale bar in B: 1 mm.

packed (Fig. 5). Reduction in FA could be due to lower fiber density, reticular formations, and small fiber tracts crossing with each other or interacting with nuclei. These factors as well as the lack of myelination and inclination angles of fibers with respect to the xy plane could reduce the measured retardance. We noticed high FA and low retardance in median fissure (Fig. 5, ROI 5). This might be attributed to high anisotropy of water diffusion in fibrous structures and low birefringence.

The optic axis orientation contrast yields the axis of tissue anisotropy in the plane perpendicular to the illumination beam. By projecting the DTI orientations onto the *en-face* (xy) plane, we obtained a substantial agreement between the orientation measurements of SOCS and DTI. Pixel-wise orientation mismatch in the white matter estimates 5.4° with a standard deviation of 32.5°. The mismatch is further reduced to 0.1° with a standard deviation of 22.6° when the thresholds of FA and retardance are elevated to include only the densely packed parallel fibers in the analysis. The ROI analyses reveal good comparability in multiple sites where unambiguous fiber axes are resolved by DTI (Fig. 8). The results are consistent with previous reports in which the accuracy of local fiber orientations in DTI was examined by histological images. Leergaard et al. (2010) performed manual tracing on myelin stained mouse brain slices to validate DTI and q-space diffusion imaging (QSI) orientations, and found a correlation greater than 0.9 in parallel fiber tracts with DTI and an average of 5 –6° deviation from QSI in crossing regions. Using a Fourier analysis, Choe et al. (2012) declared a within 10 degree difference between DTI orientations and the axonal directions revealed on microscopy images. Similar agreements of fiber orientations were also discovered between histology images and diffusion tensor microscopy on human spinal cord slices (Hansen et al., 2011).

Apart from the positive correlations discussed above, complications stand out for crossing fiber regions. SOCS is capable of revealing the orientation variations in smaller fiber tracts in the pyramid decussation and inferior olive; however, DTI orientation cannot resolve those intricate fiber geometries, yielding a noise pattern or an average effect (Fig. 9). Spatial resolution is a limiting factor in DTI. Orientation comparability becomes less reliable for fiber tracts smaller than ~500 μm. The partial volume sampling effect and the inability to resolve multiple orientations within a voxel are other known confounds in DTI (Alexander et al., 2001). The latter issue is addressed by more sophisticated techniques of dMRI, such as high angular resolution diffusion imaging (Tuch et al., 2002), q-ball imaging (Tuch, 2004) and diffusion spectrum imaging (Wedeen et al., 2008), but each will typically require significant reductions in spatial resolution in order to increase angular resolution in a comparable amount of imaging time. The optic axis orientation contrast of SOCS is currently not able to resolve multiple axes within a depth of an optical section, thus *en-face* orientation values may have a bias towards the orientation of superficial fibers. Although the optic axis orientation is restricted on the xy-plane, information about the orientation in the third dimension is implied in the retardance measure (Larsen et al., 2007; Wang et al., 2011). The fiber orientation in 3D space can be obtained by varying the illumination angle (Lu and Matcher, 2012; Ugryumova et al., 2006). In addition, computational analysis of structural images provides a complementary method for quantifying the orientations (Budde and Frank, 2012; Choe et al., 2012; Leergaard et al., 2010), which can be adapted to the 3D structural images of SOCS. Further discussion on retardance and orientation measurements can be found in Wang et al. (2011) and Wang et al. (2014). Overall, SOCS serves as an appealing tool for validating DTI orientations and the methods established in the present study can be used to interrogate other dMRI techniques that can resolve multiple orientations within a voxel.

In this study, we targeted myelinated fibers; however, the method can be adapted to visualize unmyelinated fibers, dendrites and cell bodies by increasing the lateral resolution to the level of optical coherence microscopy (OCM). The OCM was used to image individual axons and unveil the myeloarchitecture in the cortex (Leahy et al., 2013; Srinivasan et al., 2012). Previous studies on brain and peripheral nerves using OCM have reported close correlations with histology (Arous et al., 2011; Bolmont et al., 2012; Magnain et al., 2014). Therefore, the method we propose (SOCS) has the potential to bridge multi-modality investigations on the central and peripheral nervous systems to construct a hierarchal view of neuroanatomical connections from molecular to system levels, thus opening important opportunities for systematic studies on brain mapping and neural disorders.

Supplementary data to this article can be found online at http://dx.doi.org/10.1016/j.neuroimage.2014.06.032.

Acknowledgments

This work was supported in part by the Institute for Engineering in Medicine Seed Grant program and a Doctoral Dissertation Fellowship at the University of Minnesota, and research grants from the US National Institute of Health (NIH): the National Institute for Biomedical Imaging and Bioengineering (5R01EB012538, 5P41EB015896-15, R01EB006758), the National Center for Research Resources (U24RR021382), the National Institute on Aging (AG022381, 5R01AG008122-22), the National Institute for Neurological Disorders and Stroke (R01NS052585-01, 1R21NS072652-01, 1R01NS070963), and was made possible by the resources provided by Shared Instrumentation Grants 1S10RR023401, 1S10RR019307, and 1S10RR023043. Additional support was provided by the NIH Blueprint for Neuroscience Research (5U01MH093765), part of the multi-institutional Human Connectome Project. In addition, BF has a financial interest in Corticometrics, a company whose medical pursuits focus on brain imaging and measurement technologies. BF's interests were reviewed and are managed by Massachusetts General Hospital and Partners HealthCare in accordance with their conflict of interest policies.

References

Alexander, A.L., Hasan, K.M., Lazar, M., Tsuruda, J.S., Parker, D.L., 2001. Analysis of partial volume effects in diffusion-tensor MRI. Magn. Reson. Med. 45, 770–780.
Arous, J.B., Binding, J., Leger, J.F., Casado, M., Topilko, P., Gigan, S., Boccara, A.C., Bourdieu, L., 2011. Single myelin fiber imaging in living rodents without labeling by deep optical coherence microscopy. J. Biomed. Opt. 16, 1–9.
Assayag, O., Grieve, K., Devaux, B., Harms, F., Pallud, J., Chretien, F., Boccara, C., Varlet, P., 2013. Imaging of non-tumorous and tumorous human brain tissues with full-field optical coherence tomography. NeuroImage Clin. 2, 549–557.
Axer, M., Amunts, K., Grässel, D., Palm, C., Dammers, J., Axer, H., Pietrzyk, U., Zilles, K., 2011. A novel approach to the human connectome: ultra-high resolution mapping of fiber tracts in the brain. NeuroImage 54, 1091–1101.
Basser, P.J., 1995. Inferring microstructural features and the physiological state of tissues from diffusion-weighted images. NMR Biomed. 8, 333–344.
Bolmont, T., Bouwens, A., Pache, C., Dimitrov, M., Berclaz, C., Villiger, M., Wegenast-Braun, B.M., Lasser, T., Fraering, P.C., 2012. Label-free imaging of cerebral ß-amyloidosis with extended-focus optical coherence microscopy. J. Neurosci. 32, 14548–14556.
Budde, M.D., Frank, J.A., 2012. Examining brain microstructure using structure tensor analysis of histological sections. NeuroImage 63, 1–10.
Budde, M.D., Janes, L., Gold, E., Turtzo, L.C., Frank, J.A., 2011. The contribution of gliosis to diffusion tensor anisotropy and tractography following traumatic brain injury: validation in the rat using Fourier analysis of stained tissue sections. Brain 134, 2248–2260.
Caminiti, R., Carducci, F., Piervincenzi, C., Battaglia-Mayer, A., Confalone, G., Visco-Comandini, F., Pantano, P., Innocenti, G.M., 2013. Diameter, length, speed, and conduction delay of callosal axons in macaque monkeys and humans: comparing data from histology and magnetic resonance imaging diffusion tractography. J. Neurosci. 33, 14501–14511.
Choe, A.S., Stepniewska, I., Colvin, D.C., Ding, Z., Anderson, A.W., 2012. Validation of diffusion tensor MRI in the central nervous system using light microscopy: quantitative comparison of fiber properties. NMR Biomed. 25, 900–908.
Dauguet, J., Peled, S., Berezovskii, V., Delzescaux, T., Warfield, S.K., Born, R., Westin, C., 2007. Comparison of fiber tracts derived from in-vivo DTI tractography with 3D histological neural tract tracer reconstruction on a macaque brain. NeuroImage 37, 530–538.
de Boer, J.F., Milner, T.E., van Gemert, M.J., Nelson, J.S., 1997. Two-dimensional birefringence imaging in biological tissue by polarization-sensitive optical coherence tomography. Opt. Lett. 22, 934–936.
Fields, D.R., 2008. White matter in learning, cognition and psychiatric disorders. Trends Neurosci. 31, 361–370.
Hansen, B., Flint, J.J., Heon-Lee, C., Fey, M., Vincent, F., King, M.A., Vestergaard-Poulsen, P., Blackband, S.J., 2011. Diffusion tensor microscopy in human nervous tissue with quantitative correlation based on direct histological comparison. NeuroImage 57, 1458–1465.

Harsan, L.-A., Dávid, C., Reisert, M., Schnell, S., Hennig, J., von Elverfeldt, D., Staiger, J.F., 2013. Mapping remodeling of thalamocortical projections in the living reeler mouse brain by diffusion tractography. Proc. Natl. Acad. Sci. U. S. A. 110, E1797–E1806.

Huang, D., Swanson, E.A., Lin, C.P., Schuman, J.S., Stinson, W.G., Chang, W., Hee, M.R., Flotte, T., Gregory, K., Pufialito, C.A., Fujimoto, J.G., 1991. Optical coherence tomography. Science 254, 1178–1181.

Jbabdi, S., Lehman, J.F., Haber, S.N., Behrens, T.E., 2013. Human and monkey ventral prefrontal fibers use the same organizational principles to reach their targets: tracing versus tractography. J. Neurosci. 33, 3190–3201.

Kitamura, S., Kiuchi, K., Taoka, T., Hashimoto, K., Ueda, S., Yasuno, F., Morikawa, M., Kichikawa, K., Kishimoto, T., 2013. Longitudinal white matter changes in Alzheimer's disease: a tractography-based analysis study. Brain Res. 1515, 12–18.

Koyama, M.S., Di Martino, A., Kelly, C., Jutagir, D.R., Sunshine, J., Schwartz, S.J., Castellanos, F.X., Milham, M.P., 2013. Cortical signatures of dyslexia and remediation: an intrinsic functional connectivity approach. PLoS One 8, e55454.

Larsen, L., Griffin, L.D., GrÄβel, D., Witte, O.W., Axer, H., 2007. Polarized light imaging of white matter architecture. Microsc. Res. Tech. 70, 851–863.

Leahy, C., Radhakrishnan, H., Srinivasan, V.J., 2013. Volumetric imaging and quantification of cytoarchitecture and myeloarchitecture with intrinsic scattering contrast. Biomed. Opt. Express 4, 1978–1990.

Leergaard, T.B., White, N.S., de Crespigny, A., Bolstad, I., D'Arceuil, H., Bjaalie, J.G., Dale, A.M., 2010. Quantitative histological validation of diffusion MRI fiber orientation distributions in the rat brain. PLoS One 5, e8595.

Lu, Z., Matcher, S.J., 2012. Absolute fast axis determination using non-polarization-maintaining fiber-based polarization-sensitive optical coherence tomography. Opt. Lett. 37, 1931–1933.

Magnain, C., Augustinack, J.C., Reuter, M., Wachinger, C., Frosch, M.P., Ragan, T., Akkin, T., Wedeen, V.J., Boas, D.A., Fischl, B., 2014. Blockface histology with optical coherence tomography: a comparison with Nissl staining. NeuroImage 84, 524–533.

Maller, J.J., Thompson, R.H.S., Lewis, P.M., Rose, S.E., Pannek, K., Fitzgerald, P.B., 2010. Traumatic brain injury, major depression, and diffusion tensor imaging: making connections. Brain Res. Rev. 64, 213–240.

Miyata, J., Hirao, K., Namiki, C., Fukuyama, H., Okada, T., Miki, Y., Hayashi, T., Murai, T., 2007. Interfrontal commissural abnormality in schizophrenia: tractography-assisted callosal parcellation. Schizophr. Res. 97, 236–241.

Mori, S., Crain, B.J., Chacko, V.P., van Zijl, P.C., 1999. Three-dimensional tracking of axonal projections in the brain by magnetic resonance imaging. Ann. Neurol. 45, 265–269.

Nair, A., Treiber, J.M., Shukla, D.K., Shih, P., Muller, R.A., 2013. Impaired thalamocortical connectivity in autism spectrum disorder: a study of functional and anatomical connectivity. Brain 136, 1942–1955.

Pollonini, L., Patidar, U., Situ, N., Rezaie, R., Papanicolaou, A.C., Zouridakis, G., 2010. Functional connectivity networks in the autistic and healthy brain assessed using Granger causality. Conf. Proc. IEEE Eng. Med. Biol. Soc. 2010, 1730–1733.

Preibisch, S., Saalfeld, S., Tomancak, P., 2009. Globally optimal stitching of tiled 3D microscopic image acquisitions. Bioinformatics 25, 1463–1465.

Pugh, K.R., Mencl, W.E., Shaywitz, B.A., Shaywitz, S.E., Fulbright, R.K., Constable, R.T., Skudlarski, P., Marchione, K.E., Jenner, A.R., Fletcher, J.M., Liberman, A.M., Shankweiler, D.P., Katz, L., Lacadie, C., Gore, J.C., 2000. The angular gyrus in developmental dyslexia: task-specific differences in functional connectivity within posterior cortex. Psychol. Sci. 11, 51–56.

Reuter, M., Rosas, H.D., Fischl, B., 2010. Highly accurate inverse consistent registration: a robust approach. NeuroImage 53, 1181–1196.

Rosenberger, G., Nestor, P.G., Oh, J.S., Levitt, J.J., Kindleman, G., Bouix, S., Fitzsimmons, J., Niznikiewicz, M., Westin, C.F., Kikinis, R., McCarley, R.W., Shenton, M.E., Kubicki, M., 2012. Anterior limb of the internal capsule in schizophrenia: a diffusion tensor tractography study. Brain Imaging Behav. 6, 417–425.

Schmitt, A., Hasan, A., Gruber, O., Falkai, P., 2011. Schizophrenia as a disorder of disconnectivity. Eur. Arch. Psychiatry Clin. Neurosci. 261 (Suppl. 2), S150–S154.

Seehaus, A., Roebroeck, A., Chiry, O., Kim, D.S., Ronen, I., Bratzke, H., Goebel, R., Galuske, R.A., 2013. Histological validation of DW-MRI tractography in human postmortem tissue. Cereb. Cortex 23, 442–450.

Srinivasan, V.J., Radhakrishnan, H., Jiang, J.Y., Barry, S., Cable, A.E., 2012. Optical coherence microscopy for deep tissue imaging of the cerebral cortex with intrinsic contrast. Opt. Express 20, 2220–2239.

Tham, M.W., Woon, P.S., Sum, M.Y., Lee, T.S., Sim, K., 2010. White matter abnormalities in major depression: evidence from post-mortem, neuroimaging and genetic studies. J. Affect. Disord. 132, 26–36.

Thomason, M.E., Thompson, P.M., 2011. Diffusion imaging, white matter, and psychopathology. Annu. Rev. Clin. Psychol. 7, 63–85.

Tuch, D.S., 2004. Q-ball imaging. Magn. Reson. Med. 52, 1358–1372.

Tuch, D.S., Reese, T.G., Wiegell, M.R., Makris, N., Belliveau, J.W., Wedeen, V.J., 2002. High angular resolution diffusion imaging reveals intravoxel white matter fiber heterogeneity. Magn. Reson. Med. 48, 577–582.

Ugryumova, N., Gangnus, S.V., Matcher, S.J., 2006. Three-dimensional optic axis determination using variable incidence-angle polarization-optical coherence tomography. Opt. Lett. 31, 2305–2307.

Vandermosten, M., Boets, B., Poelmans, H., Sunaert, S., Wouters, J., Ghesquiere, P., 2012. A tractography study in dyslexia: neuroanatomic correlates of orthographic, phonological and speech processing. Brain 135, 935–948.

Voineskos, A.N., Lobaugh, N.J., Bouix, S., Rajji, T.K., Miranda, D., Kennedy, J.L., Mulsant, B.H., Pollock, B.G., Shenton, M.E., 2010. Diffusion tensor tractography findings in schizophrenia across the adult lifespan. Brain 133, 1494–1504.

Wang, K., Liang, M., Wang, L., Tian, L., Zhang, X., Li, K., Jiang, T., 2007. Altered functional connectivity in early Alzheimer's disease: a resting-state fMRI study. Hum. Brain Mapp. 28, 967–978.

Wang, H., Al-Qaisi, M.K., Akkin, T., 2010. Polarization-maintaining fiber based polarization-sensitive optical coherence tomography in spectral domain. Opt. Lett. 35, 154–156.

Wang, H., Black, A.J., Zhu, J., Stigen, T., Netoff, I.T., Abosch, A., Akkin, T., 2011. Reconstructing micrometer-scale fiber pathways in the brain: multi-contrast optical coherence tomography based tractography. NeuroImage 58, 984–992.

Wang, H., Zhu, J., Akkin, T., 2014. Serial optical coherence scanner for large-scale brain imaging at microscopic resolution. NeuroImage 84, 1007–1017.

Wedeen, V.J., Wang, R.P., Schmahmann, J.D., Benner, T., Tseng, W.Y., Dai, G., Pandya, D.N., Hagmann, P., D'Arceuil, H., de Crespigny, A.J., 2008. Diffusion spectrum magnetic resonance imaging (DSI) tractography of crossing fibers. NeuroImage 41, 1267–1277.